Journal of Materials Chemistry A

Molecular-Level Environments of Intercalated Chloroaluminate Anions in Rechargeable Aluminum-Graphite Batteries Revealed by Solid-State NMR Spectroscopy

Journal:	*Journal of Materials Chemistry A*
Manuscript ID	TA-ART-03-2020-002611.R1
Article Type:	Paper
Date Submitted by the Author:	11-Jun-2020
Complete List of Authors:	Xu, Jeffrey H.; City College of New York, Chemical Engineering Jadhav, Ankur; City College of New York, Chemical Engineering Turney, Damon; City College of New York, Chemical Engineering Messinger, Robert; City College of New York, Chemical Engineering

ARTICLE

Molecular-Level Environments of Intercalated Chloroaluminate Anions in Rechargeable Aluminum-Graphite Batteries Revealed by Solid-State NMR Spectroscopy

Received 00th January 20xx,
Accepted 00th January 20xx

DOI: 10.1039/x0xx00000x

Jeffrey H. Xu, Ankur L. Jadhav, Damon E. Turney, Robert J. Messinger*

Rechargeable aluminum-graphite batteries are an emerging energy storage technology with great promise: they exhibit high rate performance, cyclability, and a discharge potential of 2 V, while both electrodes are globally abundant, low cost, and inherently safe. The batteries use chloroaluminate-containing electrolytes and store charge in the graphite electrodes when molecular $AlCl_4^-$ chloroaluminate anions electrochemically intercalate within them. However, much remains to be understood regarding the ion intercalation mechanism, in part due to the challenges associated with characterizing the chloroaluminate anions themselves. Here, we use solid-state ^{27}Al nuclear magnetic resonance (NMR) spectroscopy to probe the molecular-level electronic and magnetic environments of intercalated chloroaluminate species at different stages-of-charge. The results reveal broad ^{27}Al NMR signals associated with intercalated $AlCl_4^-$ anions, reflecting high extents of local disorder. The intercalated chloroaluminate anions experience a diversity of local environments, many of which are far from the ideal crystalline-like structures often depicted in graphite staging models. Density functional theory (DFT) calculations of the total ^{27}Al isotropic shifts enable the contributions of chemical shift, ring-current effects, and quadrupolar interactions to be quantitatively disentangled. In combination, the solid-state NMR and DFT results reveal new insights into the molecular geometries and environments of $AlCl_4^-$ anions at different extents of intercalation.

Introduction

Rechargeable aluminum-graphite batteries using chloroaluminate-containing ionic liquid electrolytes have recently been demonstrated, wherein $AlCl_4^-$ chloroaluminate anions electrochemically intercalate into graphitic electrodes.[1–3] Depending on the graphite type, Al-graphite cells exhibit discharge plateaus of ca. 2 V and discharge capacities of up to 120 mAh/g.[1–9] Numerous reports have also demonstrated their ultrafast discharge/charge capabilities[2,4,5,7], long cycle lifetimes and high Coulombic efficiencies at sufficiently fast rates,[5,6,9] and a wide operational temperature range (e.g., -40°C to 120°C)[5,6]. However, further technological improvement has plateaued, in part due to limited molecular-level understanding of the ion intercalation mechanism, as the intercalation of molecular anions into graphite differs greatly from those involving atomic cations (e.g., Li^+, Na^+, etc.). Notably, there remain discrepancies among various experimental[2,6,10] and computational[11–18] studies regarding the graphite interlayer spacing and stage numbers of the intercalated compound, as well the molecular geometries and environments of the intercalant anions. Over the past few years, aluminum-graphite batteries have been studied using a variety of techniques that reveal surface properties (e.g. XPS, AFM, SEM/EDS, TEM, etc.) or bulk properties (e.g. XRD, Raman, etc.) of the graphite electrodes. However, there have been no reports thus far that utilize techniques capable of revealing bulk properties of the intercalant anions themselves within the graphite electrode. In particular, solid-state nuclear magnetic resonance (NMR) spectroscopy can directly probe the local electronic and magnetic environments of the intercalated chloroaluminate anions themselves and would be expected to shed light on the ion intercalation mechanism.

Previous studies have established solid-state NMR as a practical and fundamental tool to study ion-intercalated battery electrode materials, revealing information on their local environments and electrochemical intercalation mechanisms.[19–24] Solid-state NMR measurements are sensitive to the local magnetic and electronic environments, ion dynamics, and ion-ion or ion-framework interactions of intercalant-electrode systems. [25] For example, Guérin et al.[26] conducted *ex situ* ^7Li NMR on fully-lithiated hard carbon electrodes to distinguish covalently bonded, intercalated and pseudo-metallic lithium species. Later on, *in operando* ^7Li NMR techniques enabled phase identification of metastable phases formed upon Li^+ intercalation into silicon electrodes[27], as well as structural characterization of dendrite growth of lithium metal anodes.[28] Similarly, ^{23}Na MAS NMR techniques (both *ex situ*[29] and *in situ*[30,31]) have been used to elucidate adsorption mechanisms and dendrite formation under various electrochemical conditions. While solid-state NMR has been used to study the intercalation of molecular anions such as hexafluorophosphate (PF_6^-)[32] and bistriflimide ($TFSI^-$)[33] into graphite, to our knowledge, it has not yet been used to study the local environments of intercalated chloroaluminate anions.

Density functional theory (DFT) quantum chemical calculation are a powerful tool to aid interpretation of observable solid-state NMR signals, which are the result of different physical

[a] Department of Chemical Engineering, The City College of New York, CUNY, 160 Convent Avenue, New York, New York 10031, United States. E-mail: rmessinger@ccny.cuny.edu

[b] † Electronic Supplementary Information (ESI) available: [Solid-state NMR sample preparation, additional NICS effects, and calculated EFG Tensors]. See DOI: 10.1039/x0xx00000x

interactions. These methods have been used to calculate magnetic shielding tensors (chemical shifts) and electric field gradient (EFG) tensors[34] for systems where chemical species interact with various carbon structures such as porous carbons[35,36], polycyclic aromatic hydrocarbons[37], single-layer graphene[38] and graphite[39]. For example, Forse et al.[36] studied the effects of different structural factors on DFT-derived NMR shifts, which were used to interpret experimental ^{19}F NMR spectra of BF_4^- anions adsorbed on titanium carbide-derived carbons. DFT has also been used to compute the molecular structures and energetics of other intercalating molecular species into graphite, such as PF_6^- anions[40–42], ClO_4^- anions[42], and $TFSI^-$ anions[43], with applications for positive electrodes for lithium and sodium batteries.[40–42]

Here, we report solid-state ^{27}Al magic-angle-spinning (MAS) NMR measurements of natural graphite electrodes cycled to different states-of-charge to probe the molecular-level environments of intercalated $AlCl_4^-$ chloroaluminate species at different extents of ion intercalation. The solid-state ^{27}Al NMR results revealed broad ^{27}Al signals with varying shifts and linewidths associated with chloroaluminates in diverse local environments. To interpret the experimentally observed NMR ^{27}Al shifts, we performed DFT calculations on an [$AlCl_4^-$]-coronene bilayer model system with varying interlayer spacings to simulate structures with different $AlCl_4^-$ molecular geometries and environments. The DFT calculations were used to compute the contributions of the chemical shift, aromatic ring-current effects, and electric quadrupolar couplings on the total ^{27}Al isotropic shifts. The calculated total ^{27}Al isotropic shifts were correlated with the experimental ^{27}Al shifts to better understand the physical, molecular-level picture of intercalant-graphite-host interactions. Additional insights into the local dynamics and disorder of chloroaluminate anions intercalated into graphite were revealed by trends of the ^{27}Al longitudinal T_1 NMR relaxation times and ^{27}Al signal linewidths at different states-of-charge.

Methods

Cell assembly and electrochemical measurements. The experimental methods for electrode fabrication, cell assembly, and electrochemical testing are detailed in our previous work[4]. Briefly, composite electrodes were prepared using natural graphite flakes (Alfa Aesar, 99.9995%) and poly(vinylidene fluoride) (PVDF) binder (Sigma-Aldrich, average molecular weight 534000 g/mol) in a mass ratio of 90:10 on molybdenum (Mo) foil current collectors (Alfa Aesar, 99.95%, 0.025 mm thick). Cells were prepared using an aluminum foil negative electrode (MTI, 99.99%, 0.1-mm thick), a glass fiber separator (Whatman brand, GF/D), the graphite positive electrode, and an $AlCl_3$:[EMIm]Cl electrolyte (1.5:1 molar ratio, Iolitec, 30 µL) using polytetrafluoroethylene (PTFE) unions (Swagelok, ½-in. (12.7-mm) diameter, no. T-810-6) as airtight cell bodies and Mo current collector rods (Torrey Hills Technologies). Typical open circuit potentials for the Al-graphite cells were ca. 1.65 V. Galvanostatic cycling was performed on an Arbin LBT battery tester at 60 mA/g using upper and lower voltage cut-off limits of 2.45 V and 0.50 V, respectively.

NMR sample preparation. After the aluminum-graphite cell's desired state-of-charge was reached, it was disassembled in an argon-filled glovebox (<1 ppm O_2 and H_2O levels). Excess electrolyte was removed from the graphite electrodes by rinsing with anhydrous methanol, soaking for 5 mins, and then rinsing again. Anhydrous methanol was observed to be more effective at removing excess electrolyte than CCl_4, as measured by energy-dispersive X-ray Spectroscopy (EDS) via a Helios NanoLab 660 SEM with an Oxford EDX detector (Fig. S1). The electrode was dried in the glovebox for 20 min to allow the methanol to evaporate. The graphite was then separated from the current collector and ground by mortar and pestle and diluted with potassium bromide (Anhydrous, Sigma-Aldrich, ≥99%) at a mass ratio of 30:70 sample:KBr to improve MAS spinning stability by reducing the electrical conductivity of the composite sample. This sample:KBR mixture was then packed into 1.6-mm diameter zirconia rotors inside the argon-filled glovebox.

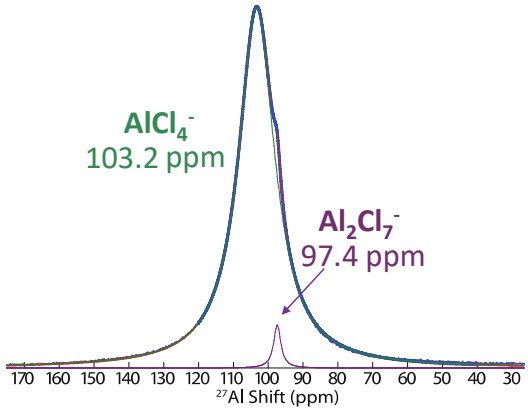

Figure 1. Liquid-state ^{27}Al single-pulse NMR spectrum of neat $AlCl_3$:[EMIm]Cl (molar ratio 1.5:1) ionic liquid electrolyte

NMR spectroscopy. Solid-state ^{27}Al NMR measurements were acquired on a Bruker AVANCE III HD 600 MHz spectrometer with a 14.1 T narrow-bore superconducting magnet operating at 156.375 MHz for ^{27}Al nuclei, respectively. A Phoenix 1.6-mm HXY MAS probehead was used. Samples were rotated at MAS rates of 10 kHz, which was limited due to the high conductivity of the graphite samples. Air at a temperature of 293.2 K was pumped through the probehead at 600 l/h to mitigate sample heating due to MAS. Samples were spun at 10 kHz MAS for 6 hours before data collection to centrifugally separate any excess free electrolyte trapped in the pores of sample (Fig. S2). Solid-state ^{27}Al single-pulse NMR measurements were conducted using π/2 radio frequency (rf) pulses of 1.9 µs (131.6 kHz rf field strength). Note that both π/12 and π/2 rf pulses yielded identical solid-state ^{27}Al NMR spectra, indicating that single-pulse experiments with π/2 rf pulses were quantitative.[44] Longitudinal (T_1) and transverse (T_2) relaxation time measurements were performed using the inversion-recovery and variable-delay spin-echo pulse sequences, respectively. Recycle delays of 0.25 s were used for all experiments, which were calibrated to ensure that all ^{27}Al spins relaxed to equilibrium (>5T_1) and that all spectra are fully quantitative. Absolute spectral intensity was normalized by sample mass. ^{27}Al shifts were referenced to a 1M aqueous solution $Al(NO_3)_3$ at 0 ppm. Spectral deconvolutions were performed with DMFit software.[45] All ^{27}Al signals associated with intercalated chloroaluminate species were modeled as a mixed

Gaussian/Lorentzian lineshape (e.g., 0.50 Gaussian:Lorentzian ratio for the dominant ^{27}Al NMR signal), while those associated with the liquid electrolyte were modeled as pure Lorentzian lineshapes.

DFT calculations. Gaussian09[46] was used to perform all ^{27}Al magnetic shielding tensors and electric field gradient tensor calculations. Ground-state DFT methods using a 6-31G(d) basis set and the hybrid B3LYP functional (Becke's three-parameter nonlocal exchange functional and Lee-Yang-Parr's correlation functional) were used for all geometry optimization and gauge-independent atomic orbital (GIAO) NMR calculations of coronene (as a model graphite layer), following Moran et al.[37] and Forse et al.[36] to optimize similar coronene structures. The coronene bilayer was constructed using an *AB* stacking (Bernal) structure and the van der Waals dispersion correction (D3) developed by Grimme et al.[47] The structures of the coronene bilayer and $AlCl_4^-$ molecule were first optimized independently. To construct the graphite intercalation compound, the optimized $AlCl_4^-$ structure was inserted in the central point of the optimized bilayer coronene structure (vertically (*c*-axis) and laterally (*a*- and *b*-axis)). Atom Groups were used to assign charges to the coronene bilayer (+1) and the $AlCl_4^-$ (-1). For calculations involving incremental changes of the bilayer coronene *d*-spacing, ion lateral-displacement, the geometry of the $AlCl_4^-$ molecule was first re-optimized using fixed carbon and aluminum atomic coordinates and a Universal Force Field (UFF) in Avogadro Molecular Editor.[48] A chemical shielding value for $[Al(H_2O)_6]^{3+}$ of 611 ppm [B3LYP/6-31G(d)] was used as the reference to convert ^{27}Al magnetic shielding values to ^{27}Al chemical shift values. The ions in the electrolyte (non-intercalated) were modeled as an $[AlCl_4^-][EMIm^+]$ ion pair using the B3LYP-D3 basis set, as recommended for DFT calculations of imidazolium-based ionic liquids.[49]

Results and Discussion

Solid-state ^{27}Al NMR measurements were conducted to reveal the molecular-level environments of the intercalated chloroaluminate species and how they change with varying cell states-of-charge (i.e., extent of ion intercalation). Subsequently, DFT calculations were performed to understand quantitatively the relative contributions of different NMR interactions to the solid-state ^{27}Al NMR shifts.

Molecular-level environments of intercalated chloroaluminate species elucidated by solid-state ^{27}Al NMR. The liquid-state single-pulse ^{27}Al NMR spectrum (Fig. 1) reveals overlapping ^{27}Al signals that can be deconvoluted into two purely Lorentzian components at 103.2 and 97.4 ppm associated with $AlCl_4^-$ and $Al_2Cl_7^-$, respectively. The relative populations of $AlCl_4^-$ and $Al_2Cl_7^-$ species, obtained by their relative integrated ^{27}Al signal intensities, were measured to be 90% and 10%, consistent with Ferrara et al.[50] The longitudinal (T_1) relaxation times were 200 and 290 μs for $AlCl_4^-$ and $Al_2Cl_7^-$, respectively. The longer ^{27}Al T_1 relaxation time for the dimeric species is due to slower stochastic fluctuations of the electric field gradient as a result of its larger size and slower molecular motions (e.g., rotations). Both ^{27}Al signals associated with the chloroaluminate anions exhibited single-exponential T_1 relaxation, as opposed to multi-exponential, consistent with fast isotropic motions in the liquid-state and relaxation behavior within the extreme narrowing limit[50]. Accordingly, the ^{27}Al transverse relaxation time (T_2) times were identical to the T_1 relaxation times.

To probe the molecular environments of intercalated $AlCl_4^-$ species intercalated within the graphitic layers, solid-state single pulse ^{27}Al MAS NMR measurements were performed on electrodes cycled to various states-of-charge (Fig. 2) corresponding to inflection points on the voltage vs. time galvanostatic cycling profiles, at which key electrochemical events associated with the formation of periodically-ordered graphite stages occur.[4] The solid-state ^{27}Al NMR spectrum of an electrode that was harvested at the open-circuit potential (non-cycled) 1.65 V 24 hours after cell assembly (point A) and rinsed with anhydrous methanol shows no ^{27}Al signal intensity, establishing that methanol successfully removed the excess electrolyte and that no solid reaction products were formed.

The solid-state ^{27}Al NMR spectra reveal ^{27}Al signals that increase in intensity upon charge and decrease in intensity upon discharge, reflective of the changing populations of chloroaluminate species intercalated within the graphite electrode (Fig. 2). The NMR spectra and their deconvolutions reveal three ^{27}Al components: (i) a main broad ^{27}Al signal, ranging from 48.8 to 78.3 ppm, associated with $AlCl_4^-$ chloroaluminate anions that are intercalated within the graphite layers, (ii) a sharp signal at ca. 103 ppm attributed to residual bulk electrolyte, and (iii) a lower-intensity broad peak centered >0 ppm whose origin is unclear, but whose shift is consistent with octahedrally-coordinated aluminum species. Note that adsorbed chloroaluminate anions compose a negligible fraction of the ^{27}Al NMR signals due to the low specific surface area of natural graphite (4.4 m^2/g, as measured by N_2 sorption) relative to the total interlayer surface area available for intercalation. As shown in our prior work[4], capacity attributed to surface effects, such as double-layer capacitive charging or faradaic electrochemical reactions of adsorbed ions, are expected to account for <1% of the total capacity. Instead, the observed capacity is due to the electrochemical intercalation of $AlCl_4^-$ anions into the graphite layers.

Analyses of the main broad ^{27}Al signal associated with intercalated $AlCl_4^-$ species reveal insights into their local environments at different states-of-charge. ^{27}Al NMR shifts and linewidths (full-width-half-maximum, FWHM, of Gaussian lineshape) are shown in Fig. 3a,b, respectively. Upon charging from the open-circuit potential of 1.65 V (point A) to 1.90 V (point B, charge time ca. 60 s at 60 mA/g), chloroaluminate anions begin to electrochemically intercalate within the graphite layers without establishing ordered graphite staging (i.e., dilute staging[51]) as evidenced *in operando* XRD measurements below 2.06 V.[10] The corresponding ^{27}Al NMR spectrum reveals a low-intensity ^{27}Al signal centered at 56.7 ppm that is broad in nature (FWHM of 108 ppm), which is associated with $AlCl_4^-$ chloroaluminate ions in distorted geometries, as discussed below. After charging to 2.25 V (point C) and 2.45 (point D), chloroaluminate species continue to intercalate, resulting in graphite interlayer expansion and ion staging. The ^{27}Al signals associated with intercalated $AlCl_4^-$ species shifts to ca. 78 ppm and its linewidths decreases, likely because the intercalated molecular anions reside in less distorted and modestly more uniform environments. The average ^{27}Al NMR shift of an intercalated chloroaluminate

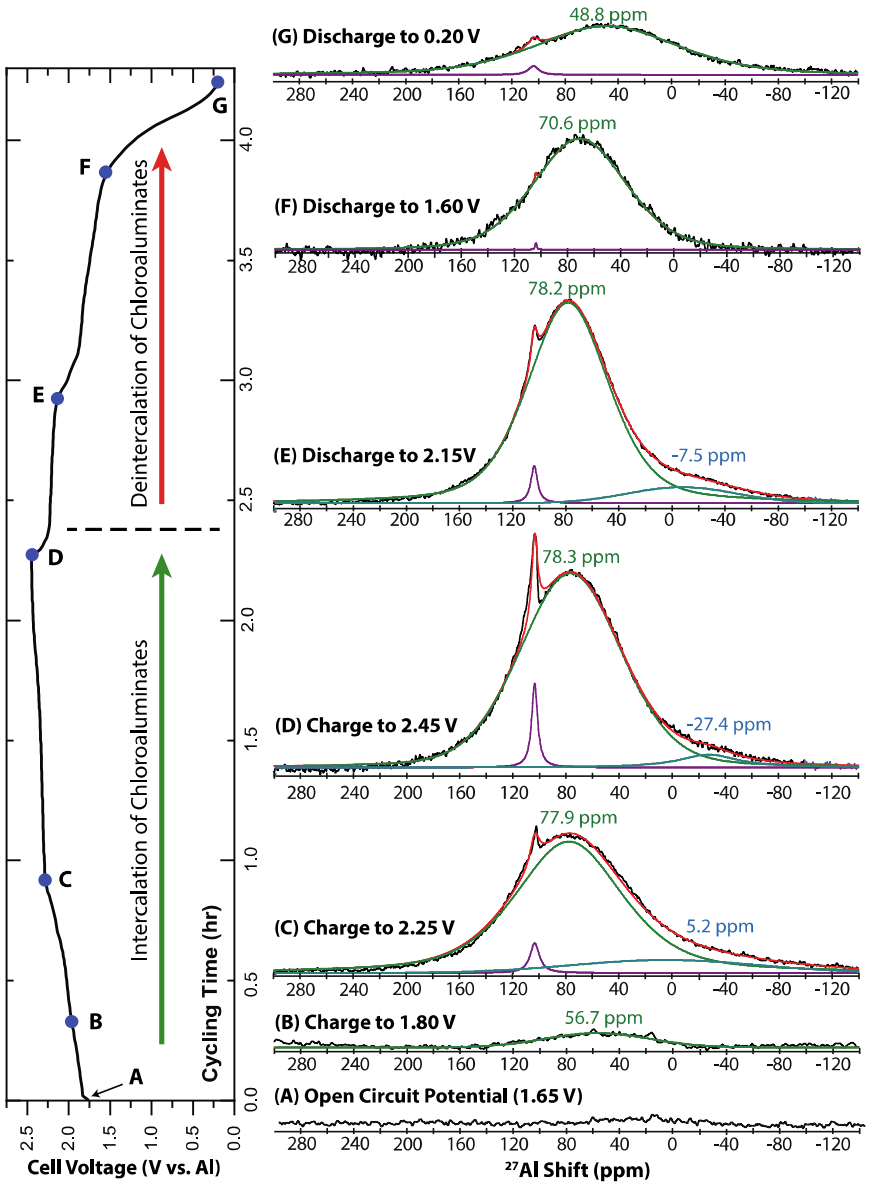

Figure 2. Solid-state ^{27}Al single-pulse MAS NMR spectra (right) of natural graphite electrodes from Al-graphite cells galvanostatically cycled to specified states-of-charge at 60 mA/g (left), acquired under conditions of 10 kHz MAS at 14.1 T. Point (A) represents an electrode from a cell that remained at the open-circuit potential for 24 h. Quantitative deconvolutions of the NMR spectra are shown. The dominant ^{27}Al signal (e.g., 78.3 ppm, Point D) is associated with molecular $AlCl_4^-$ anions intercalated into graphite.

species is 78.3 ppm (point D). Nevertheless, the broad distributions of ^{27}Al chloroaluminate environments, reflected in the broad Gaussian lineshapes (FWHM of 90 ppm, point D), are a direct manifestation of the underlying heterogeneity and disorder of the graphite structure. The intercalated chloroaluminate anions thus experience a diversity of magnetic and electronic environments, many of which are far from the idealized, crystalline-like structures often depicted in ion staging models

Upon discharge to the 2.15 V (point E), the chloroaluminate anions begin to electrochemically de-intercalate, but the average ^{27}Al shift associated with intercalated anions remains nearly identical at 78.2 ppm. Interestingly, the lineshape narrows (FWHM of 72 ppm), reflecting modestly less disordered environments. This result is consistent with preferential de-intercalation of chloroaluminate anions on the edges of the particles during this part of the discharge process. These edge-sites are expected to be more disordered, on average. Further discharge to 1.60 V (point F) results in ^{27}Al shift at 70.6 ppm, and full discharge to 0.20 V (point G) results in a ^{27}Al NMR signal of lower intensity centered at 46.8 ppm that is likely due to "trapped" chloroaluminate species in distorted environments within the graphite layers. This spectroscopic result is consistent with our prior electrochemical measurements[4], which establish additional capacity observed during the first charge, which may be associated partly or completely with trapped chloroaluminate anions. As discussed below, the ^{27}Al shifts of these trapped ions are consistent with chloroaluminate anions

in more distorted geometries, which may be expected for trapped species. These NMR results also agree with *in operando* XRD results of Wang et al.,[10] who show negligible changes in the graphite structure upon discharging from 2.45V (point D) to 2.15V (point E), but from 2.15V to 1.60V (point F) observe significant contraction of the graphite *d*-spacing that would be expected to distort ions trapped locally within the bulk graphite cathode.

The ^{27}Al longitudinal T_1 NMR relaxation times of the intercalated chloroaluminate species (Fig. 3c) yield information consistent with their molecular mobilities and the extents of local disorder. ^{27}Al longitudinal relaxation is dominated by the electric quadrupolar interaction, wherein local motions of the chloroaluminate anions cause the local electric field gradients (EFG) and hence quadrupolar interactions to fluctuate stochastically, a non-coherent process that forces the ^{27}Al spins to relax to thermal equilibrium. Hence, the ^{27}Al T_1 relaxation times are linked to molecular motions, where relaxation is most

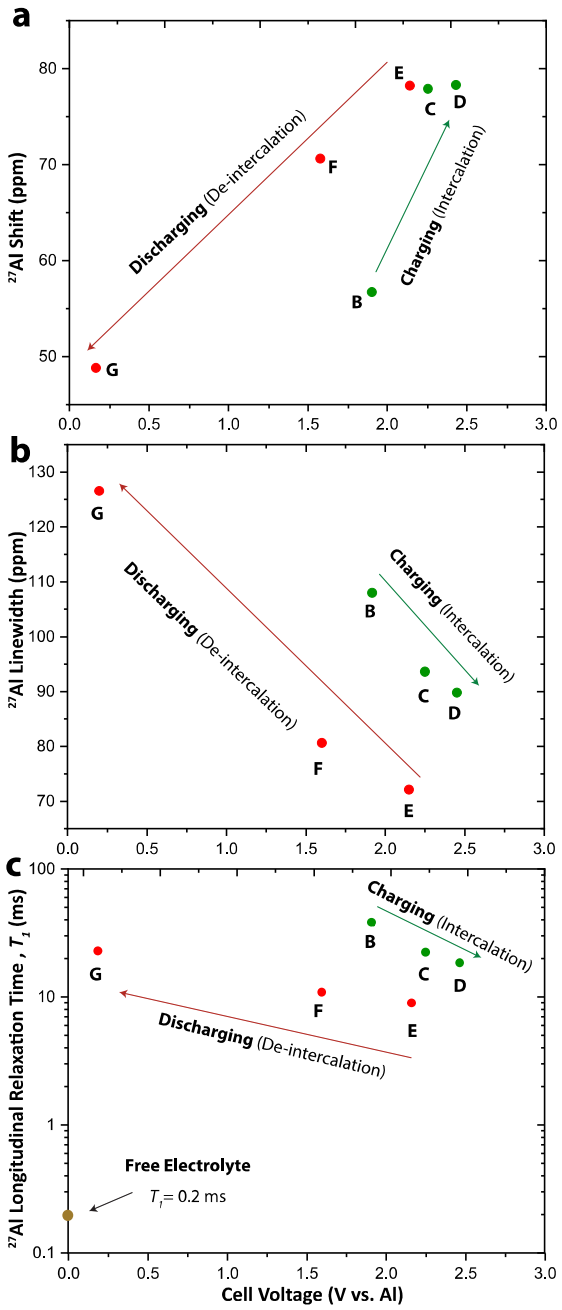

Figure 3. Analyses of the solid-state ^{27}Al NMR signals attributed to $AlCl_4^-$ anions intercalated within natural graphite. (a) Average ^{27}Al shifts, (b) ^{27}Al signal linewidths (full-width-at-half-maximum), and (c) ^{27}Al longitudinal T_1 relaxation times.

efficient (lower T_1) when the correlation time of motion is of the order of the inverse Larmor frequency ($1/\omega_0$), which is on the order of nanoseconds. Mono-exponential ^{27}Al longitudinal relaxation behavior was observed for the intercalated $AlCl_4^-$ anions with T_1 values on the order of 10 ms. These relaxation times are 2 orders-of-magnitude greater compared to the ^{27}Al T_1 of $AlCl_4^-$ ions within the bulk electrolyte (200 μs), consistent with their reduced mobilities within the graphite layers. The ^{27}Al T_1 relaxation times of the intercalated $AlCl_4^-$ anions decreased during charge (from 36.5 to 18.8 ms) and subsequently increases during discharge (from 9.3 to 23.0 ms). Interestingly, the ^{27}Al T_1 values exhibited a similar trend to the ^{27}Al linewidths, a correlation that indicates that ^{27}Al longitudinal NMR relaxation behavior is linked to the extent of local disorder. Indeed, for graphite electrodes charged to 1.90 V, 2.15 V, and 2.45 V, then discharged to 2.15 V and 1.60 V (i.e., points (B) through (F)), a smaller ^{27}Al linewidth correlates with shorter ^{27}Al T_1 relaxation times, suggesting that chloroaluminate anions in less disordered, more uniform environments exhibit greater local mobility. Note that fluctuating ^{27}Al-^{27}Al magnetic dipole-dipole couplings, arising from intermolecular interactions among neighboring intercalated chloroaluminate species, are another source of relaxation but are of secondary importance compared to intramolecular electric quadrupolar interactions.

As mentioned above, additional broad ^{27}Al NMR signals exist whose ^{27}Al shifts are consistent with octahedrally-coordinated aluminum moieties.[52] The origin of these signal is unclear. At 2.45 V (point D), the ^{27}Al signal is centered at -27.4 ppm and accounts for 5% of the overall aluminum within the electrode. While it is possible that exposure to air could result in octahedral moieties such as AlO_6, these signals only appear at higher voltages (2.15 V and above), i.e., higher extents of chloroaluminate intercalation.

In addition, solid-state ^{27}Al MAS NMR measurements were acquired on a fully intercalated graphite electrode (2.45 V) at varying carrier frequencies (±1600 ppm and ±3200 ppm) to detect possible Knight-shifted ^{27}Al signals in metallic environments. Such signals have been observed in solid-state NMR studies of lithium-ion-intercalated[26,53,54] and sodium-ion-intercalated[29,30] graphitic compounds, which indicated the reversible formation of quasi-metallic clusters due to ion aggregation at high loadings. Here, Knight-shifted ^{27}Al signals were not detected over a broad frequency range, establishing that no quasi-metallic aluminum clusters were formed. Note that aluminum metal has a ^{27}Al NMR shift of approximately 1640 ppm, as shown in a solid-state ^{27}Al single-pulse MAS NMR spectrum of metallic aluminum powder (Fig. S4). The absence of quasi-metallic aluminum is expected and consistent with the intercalation of molecular chloroaluminate anions into graphite, rather than atomic Al^{3+} cations.

Quantitative interpretations of experimental ^{27}Al NMR shifts using DFT calculations.

The intercalated chloroaluminates exhibit ^{27}Al signals that depend upon a combination of different NMR interactions: (i) chemical shift, (ii) nucleus-independent chemical shift, and (iii) electric quadrupolar couplings. We employ DFT methods to quantitatively disentangle the relative contributions of these NMR interactions to the experimental ^{27}Al NMR shifts and better understand the molecular-level environments of the intercalated chloroaluminate anions.

The total ^{27}Al isotropic NMR shift is the sum of each of these contributions:

$$\delta_{iso}^{total} = \delta_{iso}^{CS} + \delta_{iso}^{NICS} + \delta_{iso}^{2Q} \quad (1)$$

where $\boldsymbol{\delta_{iso}^{total}}$ is the total isotropic shift, $\boldsymbol{\delta_{iso}^{CS}}$ is the isotropic chemical shift, $\boldsymbol{\delta_{iso}^{NICS}}$ is the nucleus-independent chemical shift, and $\boldsymbol{\delta_{iso}^{2Q}}$ is the second-order isotropic quadrupolar shift.

The chemical shift is an intramolecular diamagnetic shielding effect; electrons that surround each nucleus circulate in an applied magnetic field, whose motions induce a magnetic field that opposes the externally applied one, causing magnetic shielding of the nucleus. The nucleus-independent chemical shift is an intermolecular diamagnetic shielding effect, where magnetic shielding arises from aromatic ring currents due to the motions of delocalized electrons in the aromatic conjugated systems. While both interactions involve magnetic shielding, only the chemical shift of a nucleus depends upon its local electronic bonding environment. The quadrupolar coupling is an electric interaction between the nuclear electric quadrupole moment of a nucleus with spin $I > 1/2$ and the local electric field gradient (EFG) at the nucleus.

The above solid-state NMR results establish that the intercalated chloroaluminate anions experience a wide variety of environments, many of which are far from those in ordered environments. This motivates the need to understand chloroaluminates in non-ideal, distorted geometries. Note that XRD only measures structures with long-range periodic ordering (i.e. they diffract) such as graphite layers with well-defined *d*-spacings that are associated with ion staging, conditions which are not necessarily achieved locally, or at low extents of intercalation. Therefore, XRD does not capture dilute staging or local disorder, while coherent diffraction of the

Table 1. DFT-computed NMR parameters for the [$AlCl_4^-$]-coronene-based bilayer system with varying interlayer spacings.

Interlayer spacing (Å)	Isotropic chemical shielding (σ_{iso}, ppm)	Isotropic chemical shift (δ_{iso}^{CS}, ppm)	EFG tensor principle component (V_{zz}, atomic units)	Quadrupolar coupling constant (C_Q, MHz)	Quadrupolar asymmetry parameter (η)	Isotropic quadrupolar shift (δ_{iso}^{2Q}, ppm)	Nucleus independent chemical shift (δ_{iso}^{NICS}, ppm)	Total Calculated Isotropic shift (δ_{iso}^{total}, ppm)
6.5	494.4	116.6	-0.484	-16.8	0.24	*-71.1*	-17.5	28.0
7	502.9	108.1	-0.377	-13.1	0.15	*-42.7*	-16.9	48.6
7.5	507.7	103.4	-0.240	-8.4	0.10	*-17.2*	-16.3	69.9
8	510.4	100.7	-0.146	-5.1	0.05	*-6.4*	-15.7	78.6
8.5	511.8	99.2	-0.0750	-2.6	0.13	*-1.7*	-15.2	82.3
9	512.5	98.5	-0.0298	-1.0	0.28	*-0.3*	-14.6	83.6
9.2	512.6	98.4	-0.0188	-0.7	0.57	*-0.1*	-14.4	83.9
9.5	512.7	98.3	0.000	0.0	0.06	*0.0*	-14.1	84.2
10	513.0	98.0	0.000	0.0	0.00	*0.0*	-13.6	84.8
10.5	513.3	97.7	0.000	0.0	0.01	*0.0*	-13.1	84.9

intercalated chloroaluminates themselves have not been reported. Furthermore, *d*-spacings derived from *in operando* XRD measurements vary[2,6,10] because they employ models that require the assumption of a single, ideal stage number *n*, rather than a more realistic mixed-stage configuration.[15]

To capture the local disorder measured experimentally by solid-state NMR, we modeled chloroaluminates intercalated in between coronene or coronene-like sheets with decreasing interlayer spacings (from 10.5 Å to 6.5 Å, Fig. 4) to simulate how they deviate from the tetrahedral geometry due to interactions with the van der Waals forces between graphite layers.[55] For each interlayer spacing, the $AlCl_4^-$ molecular geometry is re-optimized to minimize the formation energy of the bilayer-[$AlCl_4^-$] structure. Note that structural or chemical defects of graphite, such as edges, carbon vacancies, and oxygen impurities, are other sources of disorder that are not modeled here.

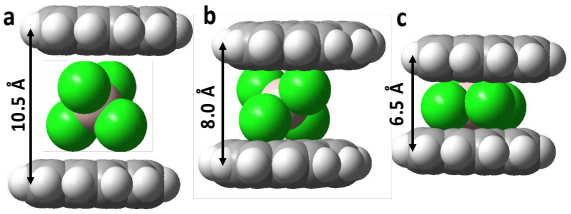

Figure 4. Space-filling models of DFT-optimized [$AlCl_4^-$]-coronene bilayer structures with varying interlayer spacings and degrees of geometric distortion. Van der Waals volumes are shown for the $AlCl_4^-$ anion.

Calculated Chemical Shift. To compute the ^{27}Al chemical shift, first the principal components (σ_{xx} , σ_{yy} and σ_{zz}) of the chemical shielding tensor σ within its principle axis system are calculated for the optimized structure. The isotropic shielding constant

$$\sigma_{iso} = \frac{\sigma_{xx} + \sigma_{yy} + \sigma_{zz}}{3} \quad (2)$$

describes the magnetic shielding at the aluminum nucleus in the $AlCl_4^-$ anion. The DFT-calculated chemical shielding constant σ_{iso} can be converted to a DFT-calculated isotropic chemical shift δ_{iso}^{CS} via

$$\delta_{iso}^{CS} = \sigma_{\mathrm{iso}}^{reference} - \sigma_{\mathrm{iso}} \quad (3)$$

where $\sigma_{\mathrm{iso}}^{reference}$ is the DFT-calculated shielding of the ^{27}Al NMR reference standard (For $[Al(H_2O)_6]^{3+}$, $\sigma_{\mathrm{iso}}^{reference} = 611$ ppm).[56] Using this reference standard yields $\delta_{iso}^{AlCl_4^-} = 102$ ppm for an $AlCl_4^-$ anion, similar to the experimental ^{27}Al NMR shift of 103.2 ppm for $AlCl_4^-$ in the neat electrolyte.

The ^{27}Al chemical shift was modeled using coronene bilayer interlayer spacings from 10.5 Å to 6.5 Å (Table 1, Fig. 5a). At a large graphite *d*-spacing of 10.5 Å (Fig. 5a), the optimized molecular geometry is tetrahedral, yielding a high shielding constant (σ_{iso} = 513.3 ppm) that corresponds to a ^{27}Al isotropic chemical shift δ_{iso}^{CS} of 97.7 ppm. As the interlayer spacing is reduced, the $AlCl_4^-$ experiences increasing deviations from the tetrahedral geometry. For example, enforcing an interlayer spacing of 6.5 Å results in near-planar geometry and a lower shielding constant (σ_{iso} = 494.4 ppm) that corresponds to a greater ^{27}Al isotropic chemical shift δ_{iso}^{CS} of 116.6 ppm. This higher chemical shift value is a result of decreased electron density around the ^{27}Al nucleus due to altered bond lengths and bond angles from those of the tetrahedral geometry of $AlCl_4^-$.

Calculated Nucleus-Independent Chemical Shift (NICS). To estimate the shift contribution due to ring-current effects from the graphite layers, nucleus-independent chemical shift (NICS)[35,36] calculations were performed using a "ghost" atom to probe the local effective magnetic field between a bilayer coronene-based structure. Since aromatic ring-currents have an effect whose magnitude depends on the domain size of the graphene sheets,[36] a coronene bilayer model will underestimate the magnitude of the NICS value experienced by intercalated ACl_4^- anions (Fig. S3a). Therefore, larger coronene-based graphene sheets (here, lateral diameters of 23.7 Å) were used to better simulate the larger *ab* crystallite dimensions of natural graphite.[4] NICS values $\boldsymbol{\delta_{iso}^{NICS}}$ were computed for interlayer spacing varying from 10.5 Å to 6.5 Å (Table 1, Figure 4b). Note that NICS values does not require a reference nucleus. As the interlayer spacing decreased, the magnitude of NICS increased due increased molecular proximity of the ^{27}Al nucleus and the coronene-based sheets. For example, bilayers with interlayer spacings of 10.5 and 6.5 Å yielded NICS values of -13.1 and -17.5 ppm, respectively (Table 1). Note that ring currents contribute to magnetic shielding and serve to reduce the ^{27}Al isotropic shift, which are in qualitative agreement with the fact that the ^{27}Al NMR shifts of the intercalated $AlCl_4^-$ anions resonate at lower frequency compared to that of the $AlCl_4^-$ in the bulk electrolyte (Fig 1).

Additionally, the NICS values varied with lateral displacement of the atom for a constant *d*-spacing, since ring-currents induce shielding above/below the ring and deshielding in the periphery of the ring. For example, using a coronene bilayer model to illustrate this concept with an interlayer spacing of 9.0 Å, the NICS value is -4.8 ppm at the center, but more deshielded (-0.2 ppm) at the periphery (Fig. S3b). The shift contribution from lateral displacement of anions are expected to be proportionally small, since edge sites are only a small fraction of all available interlayer space. Therefore, we ignore this effect and assume the central position (*x*=0) of the bilayer model for subsequent analyses.

Calculated Quadrupolar Shift. Distortions of the molecular geometry of the intercalated $AlCl_4^-$ anion will influence the electric quadrupolar coupling interaction between the ^{27}Al nuclei and the local electric field gradients (EFG), which will contribute to the total ^{27}Al isotropic shift.[57,58] DFT calculations of the optimized molecular structure enable the EFG tensor to be computed at the aluminum nucleus.[34] The Hamiltonian describing this interaction is

$$H_Q = \frac{eQ}{2I(2I-I)\hbar} \mathbf{I} \cdot \mathbf{V} \cdot \mathbf{I} \quad (4)$$

where e is the elementary charge, Q is the nuclear electric quadrupole moment of the nucleus (For ^{27}Al, Q = 148.2 ± 0.5 mb)[59], $\hbar$ is reduced Planck's constant, I is the nuclear spin quantum number, $\mathbf{I}$ is the nuclear spin operator, and $\mathbf{V}$ is the EFG tensor. The nuclear quadrupole coupling constant (C_Q) quantifies the magnitude of the quadrupolar interaction via

$$C_Q = \frac{eQV_{zz}}{h} \quad (5)$$

Where h is Planck's constant, V_{zz} is the principal component (eigenvalue) within its principle axis system with the largest magnitude of the traceless EFG tensor (by convention, $|V_{zz}| \geq$

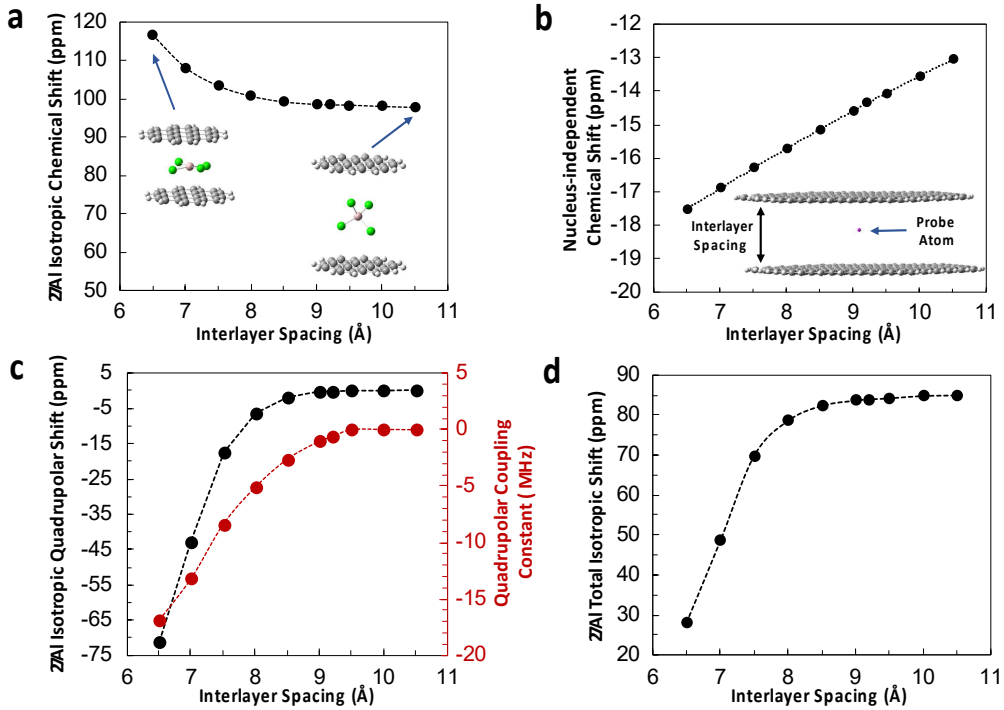

Figure 5. DFT-calculated ^{27}Al parameters of [$AlCl_4^-$]-coronene-based bilayer system with varying interlayer spacing. (a) ^{27}Al isotropic chemical shift (δ_{iso}^{CS}) (inset: optimized structures), (b) nucleus-independent chemical shift (δ_{iso}^{NICS}), (c) ^{27}Al nuclear quadrupolar shift (black, δ_{iso}^{2Q}) and coupling constant (red, C_Q), (d) ^{27}Al total isotropic shift (δ_{iso}^{total}). Dashed lines are shown to guide the eye.

$|V_{yy}| \geq |V_{xx}|$)[60,61]. The EFG tensor is also characterized by the quadrupolar asymmetry parameter η defined as

$$\eta = \frac{V_{xx}-V_{yy}}{V_{zz}} \quad (6)$$

The quadrupolar interaction can be expressed as a first-order and second-order perturbation to the Zeeman Hamiltonian.[58] The first-order term splits the spectrum into 2*I*-1 satellite lines. This term does not affect the central transition and its effects are averaged by MAS.[57] The second-order term is not completely removed by MAS and will alter the shift of the central transition[62]. The observable isotropic quadrupolar shift (δ_{iso}^{2Q}) can be predicted from the DFT-calculated quadrupolar parameters η and C_Q (Table 1) for a polycrystalline sample via

$$\delta_{iso}^{2Q}\,[ppm] = -\frac{3}{40}\left(\frac{C_Q}{\omega_L}\right)^2 \frac{I(I+1)-\frac{3}{4}}{I^2(2I-1)^2}\left(1+\frac{\eta^2}{3}\right) * 10^6 \quad (7)$$

where ω_L is the Larmor frequency of the ^{27}Al nuclei.[58,60,63]

The second-order ^{27}Al quadrupolar shifts were computed using coronene bilayer interlayer spacings that varied from 10.5 Å to 6.5 Å (Table 1, Fig. 5c). When the graphite *d*-spacing is 10.5 Å, the tetrahedral geometry of the optimized $AlCl_4^-$ ion yields a C_Q of ca. 0 MHz (Fig. 5c) and therefore a negligible δ_{iso}^{2Q}. When the graphite interlayer spacing decreases, the increasing deviation from the tetrahedral geometry increases the EFG. For example, at 6.5 Å, DFT calculations yielded a higher V_{zz} value of -0.48 (Table 1). The large EFG indicates high deviation from the symmetric, tetrahedral geometry of the energy-optimized $AlCl_4^-$ structure, yielding a large C_Q of 116.8 MHz (Table 1).[11,55] Consequently, the large isotropic quadrupolar shift δ_{iso}^{2Q} of -71.1 ppm will shift the NMR signal to lower frequency.

Calculated Total ^{27}Al Isotropic Shift. The calculated total isotropic shift δ_{iso}^{total} is the sum of the individual contributions modelled above (equation 1), whose values (Table 1, Fig. 5d) can be compared to the average experimental ^{27}Al NMR shifts (Fig 3a). When the interlayer spacing is decreased from 9.5 Å to 6.5 Å, the calculated ^{27}Al shift decreases from 84.2 to 28.8 pm, respectively (Table 1). The reported graphite *d*-spacings for chloroaluminate-intercalate graphite electrodes range from ca. 8.8 Å to 10.8 Å (obtained via DFT[11,15,18], XRD[6,10] and molecular dynamics (MD) simulations[14,55]). For example, *in operando* XRD measurements by Wang et al.[10] indicate that chloroaluminate-intercalated graphite at full charge exhibit long-range ordering with *d*-spacing of 9.2 Å. If we also assume an average interlayer spacing of ca. 9.2 Å, then the total calculated ^{27}Al isotropic shift δ_{iso}^{total} is 83.9 ppm, or 5.6 ppm greater than the average experimental ^{27}Al NMR shift of 78.3 ppm. This difference in absolute shift is discussed below. The trend in calculated ^{27}Al shifts at different interlayer spacings reveals insights into how the local environments of intercalated chloroaluminate change in distorted geometries.

Each calculated ^{27}Al shift δ_{iso}^{total} captures the local electronic and magnetic environments at the ^{27}Al nucleus when analyzed in terms of the underlying shifts δ_{iso}^{CS}, δ_{iso}^{2Q} and δ_{iso}^{NICS}, enabling the dominant contributions to be disentangled among competing effects. For example, an $AlCl_4^-$ anion intercalated within a coronene bilayer at an interlayer spacing of 6.5 Å has a highly-deshielded δ_{iso}^{CS} due to its near-planar geometry (δ_{iso}^{CS} = 116.6

ppm), reflective of changes in intramolecular bond lengths and angles compared to tetrahedral geometry. Simultaneously, this distortion results in a large EFG and hence a large second-order quadrupolar shift (δ_{iso}^{2Q}= -71.1 ppm). Meanwhile, the molecular proximity between the ^{27}Al nucleus and the coronene rings induces strong ring-current effects (δ_{iso}^{NICS}= -17.5 ppm). Collectively, these effects decrease the total ^{27}Al shift to lower values (δ_{iso}^{total} = 28.0 ppm).

The discrepancies between the calculated and average experimental ^{27}Al NMR shifts are a result of the simplicity of the DFT model, which differ by approximately 5 to 6 ppm for the fully intercalated electrodes (2.45V) assuming an interlayer spacing of 9 to 10 Å. First, NICS values due to ring-current effects are expected to be larger (more negative ppm values) as the diameters of the coronene-like sheets increase. When the diameters of the coronene-like sheets increase, the DFT-calculated NICS values begin to asymptote, approaching a value of approximately 15 ppm (Fig. 6). Adding parallel graphene sheets above and below the bilayer to simulate graphite staging would also add an additional correction. Second, the model consists of an isolated $AlCl_4^-$ molecule and therefore neglects intermolecular interactions among adjacent intercalated anions. Intermolecular interactions may affect the local molecular geometries of $AlCl_4^-$ anions, perturbing their chemical and quadrupolar shifts. Note that homonuclear ^{27}Al–^{27}Al magnetic dipole-dipole couplings among intercalated $AlCl_4^-$ molecules will not affect the ^{27}Al isotropic shift, as the dipolar Hamiltonian is traceless, but may still contribute to line broadening at 10 kHz MAS. Similarly, bulk magnetic susceptibility (BMS) effects[25,64–66], which arise from electron-nuclear dipolar coupling interactions and result in local magnetic field inhomogeneities, are not expected to affect appreciably the ^{27}Al shift. Anisotropic BMS effects due to the ellipsoidally-shaped (non-spherical) graphite particles could in principle alter the isotropic shift[65], though such effects are expected to be negligible at 10 kHz MAS. Notably, the residual electrolyte in contact with the graphite particle surfaces (^{27}Al signal at 103 ppm, Fig. 2) resonates at the same frequency as the neat electrolyte (Fig. 1), indicating that BMS effects do not contribute appreciably to the shift.

The range of DFT-calculated ^{27}Al isotropic NMR shifts (Table 1) is consistent with the broad ^{27}Al NMR linewidths observed experimentally. Each calculated δ_{iso}^{total} value represents a single $AlCl_4$- environment, whereas experimentally broad distributions of local ^{27}Al environments are observed that reflect heterogeneity that may be understood, in part, by variations in local $AlCl_4^-$ molecular geometries and local interlayer spacings. This distinction is manifested in the significant difference between the measured ^{27}Al transverse T_2 NMR relaxation times and apparent time T_2^* associated with Fourier transform of the free induction decay (FID) under MAS alone, i.e., the linewidth. For example, the graphite electrode charged to 2.45 V (Figure 2d) has a measured ^{27}Al T_2 of 660 μs, while the value calculated from the linewidth[67] alone (90 ppm, or 54 kHz, point D in Fig. 3b) yields a much shorter T_2* value of 5.9 μs. While dephasing of phase coherence can be the result of multiple effects, to a first approximation, the linewidth of a single intercalated $AlCl_4^-$ environment is estimated to be 2 orders-of-magnitude narrower than the broad ^{27}Al signal observed.

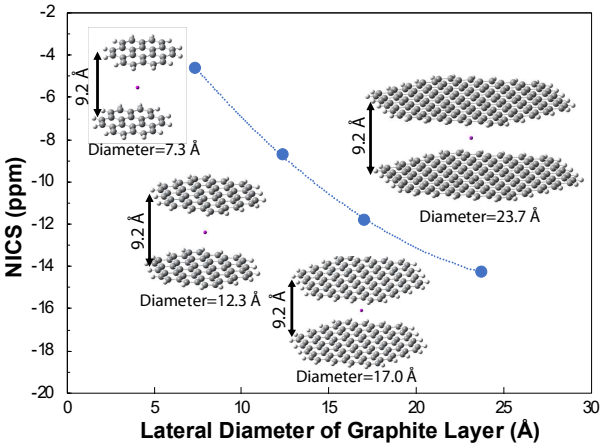

Figure 6. Nucleus-independent chemical shift (NICS) values, associated with ring-current effects calculated for coronene-like bilayer models with increasing lateral dimensions. The interlayer spacing is fixed at 9.2 Å.

Chloroaluminate Anion Intercalation Mechanism. By analyzing the experimental solid-state NMR measurements in conjunction with the theoretical quantum chemical calculations, a physical picture emerges of chloroaluminate ion intercalation into graphite. When the cell is initially charged to 1.90 V (point B, Fig. 2), the ^{27}Al NMR shift at 56.7 ppm indicates that the average local geometry of an intercalated $AlCl_4^-$ anion is highly distorted, compared to tetrahedral configurations, presumably because the ions must overcome the van der Waals forces necessary to open the graphite interlayers. Indeed, at this potential, dilute (non-ordered) graphite staging occurs,[51,68] while non-diffusion-limited ion intercalation suggests shallow penetration depths.[4] The results indicate that before the graphite layers expand to form ordered stages, the intercalating ions adapt distorted molecular geometries, which may be a key component to understanding the high-rate capabilities demonstrated for these batteries. Increasing the cell voltage to 2.25 V (point C) and then 2.45 V (point D) results in greater extents of $AlCl_4^-$ intercalation and ^{27}Al NMR shifts of ca. 78 ppm. At these points, chloroaluminate anions occupy interlayers that are greatly expanded due to their large size. The ^{27}Al NMR shifts suggesting that the larger interlayer spacings permit $AlCl_4$-anions with less distorted, near-tetrahedral geometries, which in particular reduces the local EFG and hence quadrupolar shift. Discharge to 2.15 V results in ion deintercalation yet the average ^{27}Al NMR shift remains ca. 78 ppm (point E), indicating similar average chloroaluminate environments. During discharge to 1.60 V (point F), further ion de-intercalation occurs and the ^{27}Al NMR decreases to 70.6 ppm, indicating that the average $AlCl_4^-$ anion is slightly distorted. Further discharge to 0.20 V (point G, Fig. 2) will de-intercalate the majority of $AlCl_4^-$ ions, though some trapped ions remain[4] due to the contraction of the graphite *d*-spacing to 3.3 Å upon full discharge, as shown by *in operando* XRD.[10] These trapped $AlCl_4^-$ anions exhibit average ^{27}Al NMR shifts of 48.8 pm, consistent with highly distorted geometries and large EFGs at the ^{27}Al nuclei that would decrease the ^{27}Al isotropic shift.

Conclusions

Solid-state ^{27}Al MAS NMR spectroscopy was used to probe the molecular-level environments of chloroaluminate anions intercalated within graphite electrodes at different stages of charge. The broad ^{27}Al NMR signals of the intercalated chloroaluminate anions reveal experimentally the breadth of local disorder and non-ideal staging of the graphite intercalation electrode, both of which are not captured in diffraction analyses or ideal staging models. The ^{27}Al NMR shifts and linewidths vary with different extents of ion intercalation. DFT calculations were performed to interpret the ^{27}Al NMR shifts in terms of local electronic and magnetic environments. The intercalant-electrode system was modeled as an $[AlCl_4^-]$-coronene bilayer structure, where the interlayer spacing was varied to simulate environments that distort the molecular geometry of the $AlCl_4^-$ anion. The DFT calculations enable the total ^{27}Al isotropic NMR shifts to be understood quantitatively in terms of chemical shift, ring-current effects (nucleus-independent chemical shift), and electric quadrupolar couplings. The results establish that the high extents of local disorder observed in the solid-state ^{27}Al NMR spectra are in large part due to distributions of chloroaluminate anions in different molecular configurations. In addition, the results suggest that the chloroaluminate anions can intercalate even before the graphite layers expand to form ordered stages by adapting distorted molecular geometries, which may be a key component to understanding the high-rate capabilities demonstrated in Al-graphite batteries. The solid-state ^{27}Al NMR results establish unambiguously the presence of "trapped" chloroaluminate anions after discharge (ion de-intercalation), which reside in the most distorted environments and reduce the capacity of the electrode in subsequent cycles. Overall, the combined solid-state NMR and DFT results reveal a more nuanced molecular-level understanding of the local environments of intercalated chloroaluminate anions, establishing large extents of local disorder far from the ideal crystalline-like structures often depicted in graphite staging models.

Conflicts of Interest

The authors declare no conflicts of interest.

Acknowledgements

The authors gratefully acknowledge support from the U.S. National Science Foundation (NSF) under grant no. CBET-170692. The authors thank Professor Alexander C. Forse (University of Cambridge, UK) for fruitful discussions regarding DFT modeling and NMR parameter calculations. NMR measurements were performed at the City University of New York (CUNY) Advanced Science Research Center. DFT calculations were performed at the CUNY High Performance Computing Center at the College of Staten Island, which is supported in part by NSF awards CNS-0958379, CNS-0855217, and ACI-1126113.

Notes and references

1 D. Wang, C. Wei, M. Lin, C. Pan, H. Chou, H. Chen, M. Gong, Y. Wu, C. Yuan, M. Angell, Y. Hsieh, Y. Chen, C. Wen, C. Chen, B. Hwang, C. Chen and H. Dai, *Nat. Commun.*, 2017, **8**, 1–7.

2 M.-C. C. Lin, M. Gong, B. Lu, Y. Wu, D.-Y. Y. Wang, M. Guan, M. Angell, C. Chen, J. Yang, B.-J. J. Hwang and H. Dai, *Nature*, 2015, **520**, Pages: 324–328.

3 H. Sun, W. Wang, Z. Yu, Y. Yuan, S. Wang and S. Jiao, *Chem. Commun.*, 2015, **51**, 11892–11895.

4 J. H. Xu, D. E. Turney, A. L. Jadhav and R. J. Messinger, *ACS Appl. Energy Mater.*, 2019, **2**, 7799–7810.

5 H. Chen, H. Xu, S. Wang, T. Huang, J. Xi, S. Cai, F. Guo, Z. Xu, W. Gao and C. Gao, *Sci. Adv.*, 2017, **3**, eaao7233.

6 C.-J. Pan, C. Yuan, G. Zhu, Q. Zhang, C.-J. Huang, M.-C. Lin, M. Angell, B.-J. Hwang, P. Kaghazchi and H. Dai, *Proc. Natl. Acad. Sci.*, 2018, **115**, 5670–5675.

7 L. Zhang, L. Chen, H. Luo, X. Zhou and Z. Liu, *Adv. Energy Mater.*, 2017, **2**, 1700034.

8 K. V. Kravchyk, S. Wang, L. Piveteau and M. V. Kovalenko, *Chem. Mater.*, 2017, **29**, 4484–4492.

9 Y. Wu, M. Gong, M.-C. C. Lin, C. Yuan, M. Angell, L. Huang, D.-Y. Y. Wang, X. Zhang, J. Yang, B.-J. J. Hwang and H. Dai, *Adv. Mater.*, 2016, **28**, 9218–9222.

10 D.-Y. Y. Wang, S.-K. K. Huang, H.-J. J. Liao, Y.-M. M. Chen, S.-W. W. Wang, Y.-T. T. Kao, J.-Y. Y. An, Y.-C. C. Lee, C.-H. H. Chuang, Y.-C. C. Huang, Y.-R. R. Lu, H.-J. J. Lin, H.-L. L. Chou, C.-W. W. Chen, Y.-H. H. Lai and C.-L. L. Dong, *Carbon*, 2019, **146**, 528–534.

11 Y. Gao, C. Zhu, Z. Chen and G. Lu, *J. Phys. Chem. C*, 2017, **121**, 7131–7138.

12 M. S. Wu, B. Xu, L. Q. Chen and C. Y. Ouyang, *Electrochim. Acta*, 2016, **195**, 158–165.

13 P. Bhauriyal, A. Mahata and B. Pathak, *J. Phys. Chem. C*, 2017, **121**, 9748–9756.

14 M. L. Agiorgousis, Y.-Y. Sun and S. Zhang, *ACS Energy Lett.*, 2017, 689–693.

15 Q. Wang, D. Zheng, L. He and X. Ren, *Phys. Rev. Appl.*, 2019, **12**, 1.

16 M. S. Wu, B. Xu and C. Y. Ouyang, *Electrochim. Acta*, 2017, **223**, 137–139.

17 S. C. Jung, Y. J. Kang and Y. K. Han, *Electrochim. Acta*, 2017, **223**, 135–136.

18 J. Li, Q. Liu, A. Flores, J. Lemmon and T. Bligaard, , DOI:10.1039/c9cp06394c.

19 T. Cosgrove, B. W. Copping and R. A. Jarvis, *J. Colloid Interface Sci.*, 1983, **96**, 214–221.

20 R. K. Harris, T. V Thompson, P. R. Norman and C. Pottage, 1999, **37**, 1425–1430.

21 L. Trognko, H. Wang, N. M. Trease, J. M. Griffin, P.-L. Taberna, C. P. Grey, P. Simon and A. C. Forse, *J. Am. Chem. Soc.*, 2013, **135**, 18968–18980.

22 M. Oschatz, L. Borchardt, F. Hippauf, W. Nickel, S. Kaskel and E. Brunner, *Annu. Reports NMR Spectrosc.*, 2016, **87**, 237–318.

23 H. Wang, T. K. J. Köster, N. M. Trease, J. Segalini, P.-L. Taberna, P. Simon, Y. Gogotsi and C. P. Grey, *J. Am. Chem. Soc.*, 2011, 19270–19273.

24 M. Deschamps, E. Gilbert, P. Azais, E. Raymundo-Piñero, M. R. Ammar, P. Simon, D. Massiot and F. Béguin, *Nat. Mater.*, 2013, **12**, 351–8.

25 O. Pecher, J. Carretero-gonza, K. J. Gri and C. P. Grey, , DOI:10.1021/acs.chemmater.6b03183.

26 K. Guérin, M. Ménétrier, A. Février-Bouvier, S. Flandrois, B. Simon and P. Biensan, *Solid State Ionics*, 2000, **127**, 187–198.

27 B. Key, R. Bhattacharyya, M. Morcrette, V. Seznéc, J. M. Tarascon and C. P. Grey, *J. Am. Chem. Soc.*, 2009, **131**, 9239–9249.

28 R. Bhattacharyya, B. Key, H. Chen, A. S. Best, A. F. Hollenkamp and C. P. Grey, *Nat. Mater.*, 2010, **9**, 504–510.

29 K. Gotoh, T. Ishikawa, S. Shimadzu, N. Yabuuchi, S. Komaba, K. Takeda, A. Goto, K. Deguchi, S. Ohki, K. Hashi, T. Shimizu and H. Ishida, *J. Power Sources*, 2013, **225**, 137–140.

30 J. M. Stratford, P. K. Allan, O. Pecher, P. A. Chater and C. P. Grey, *Chem. Commun.*, 2016, **52**, 12430–12433.

31 P. M. Bayley, N. M. Trease and C. P. Grey, *J. Am. Chem. Soc.*, 2016, **138**, 1955–1961.

32 G. R. Miller, H. A. Resing, M. J. Moran, L. Banks, F. L. Vogel, A. Pron and D. Billaud, *Synth. Met.*, 1983, **8**, 77–82.
33 K. V. Kravchyk, P. Bhauriyal, L. Piveteau, C. P. Guntlin, B. Pathak and M. V. Kovalenko, *Nat. Commun.*, , DOI:10.1038/s41467-018-06923-6.
34 R. W. Schurko, R. E. Wasylishen and A. D. Phillips, *J. Magn. Reson.*, 1998, **133**, 388–394.
35 Y. Z. Xing, Z. X. Luo, A. Kleinhammes and Y. Wu, *Carbon*, 2014, **77**, 1132–1139.
36 A. C. Forse, J. M. Griffin, V. Presser, Y. Gogotsi and C. P. Grey, *J. Phys. Chem. C*, 2014, **118**, 7508–7514.
37 D. Moran, F. Stahl, H. F. Bettinger, H. F. Schaefer and P. v. R. Schleyer, *J. Am. Chem. Soc.*, 2003, **125**, 6746–6752.
38 M. H. Ghatee and F. Moosavi, *J. Phys. Chem. C*, 2011, **115**, 5626–5636.
39 F. A. L. de Souza, A. R. Ambrozio, E. S. Souza, D. F. Cipriano, W. L. Scopel and J. C. C. Freitas, *J. Phys. Chem. C*, 2016, **120**, 27707–27716.
40 S. Miyoshi, T. Akbay, T. Kurihara, T. Fukuda, A. T. Staykov, S. Ida and T. Ishihara, *J. Phys. Chem. C*, 2016, **120**, 22887–22894.
41 H. J. Liao, Y. M. Chen, Y. T. Kao, J. Y. An, Y. H. Lai and D. Y. Wang, *J. Phys. Chem. C*, , DOI:10.1021/acs.jpcc.7b08429.
42 K. Tasaki, *J. Phys. Chem. C*, 2014, **118**, 1443–1450.
43 C. J. Yu, U. S. Ri, G. C. Ri and J. S. Kim, *Phys. Chem. Chem. Phys.*, 2018, **20**, 14124–14132.
44 D. Fenzke, D. Freude, T. Fröhlich and J. Haase, *Chem. Phys. Lett.*, 1984, **111**, 171–175.
45 D. Massiot, F. Fayon, M. Capron, I. King, S. Le Calvé, B. Alonso, J. O. Durand, B. Bujoli, Z. Gan and G. Hoatson, *Magn. Reson. Chem.*, 2002, **40**, 70–76.
46 D. J. F. M. J. Frisch, G. W. Trucks, H. B. Schlegel, G. E. Scuseria, M. A. Robb, J. R. Cheeseman, G. Scalmani, V. Barone, G. A. Petersson, H. Nakatsuji, X. Li, M. Caricato, A. Marenich, J. Bloino, B. G. Janesko, R. Gomperts, B. Mennucci, H. P. Hratchian, J. V. Ort, 2016.
47 S. Grimme, J. Antony, S. Ehrlich and H. Krieg, *J. Chem. Phys.*, , DOI:10.1063/1.3382344.
48 M. D. Hanwell, D. E. Curtis, D. C. Lonie, T. Vandermeersch, Z. Eva and G. R. Hutchison, *J. Cheminform.*, 2012, 4–17.
49 S. Grimme, W. Hujo and B. Kirchner, *Phys. Chem. Chem. Phys.*, 2012, **14**, 4875–4883.
50 C. Ferrara, V. Dall'Asta, V. Berbenni, E. Quartarone and P. Mustarelli, *J. Phys. Chem. C*, 2017, **121**, 26607–26614.
51 R. B. Smith, E. Khoo and M. Z. Bazant, *J. Phys. Chem. C*, 2017, **121**, 12505–12523.
52 M. Haouas, F. Taulelle and C. Martineau, *Prog. Nucl. Magn. Reson. Spectrosc.*, 2016, **94**–**95**, 11–36.
53 E. Sequoia, M. Nucldaire, L. Interstitiel and G. J. Conard, 1977, **31**, 173–176.
54 M. Letellier, F. Chevallier, F. Béguin, E. Frackowiak and J. N. Rouzaud, *J. Phys. Chem. Solids*, 2004, **65**, 245–251.
55 P. Bhauriyal, A. Mahata and B. Pathak, *Phys. Chem. Chem. Phys.*, 2017, **19**, 7980–7989.
56 V. P. Tarasov and G. A. Kirakosyan, *Russ. J. Inorg. Chem.*, 2008, **53**, 2048–2081.
57 P. P. Man, *Encycl. Magn. Reson.*, 2011, 1–10.
58 A. Samoson, *Chem. Phys. Lett.*, 1985, **119**, 29–32.
59 A. Aerts and A. Brown, *J. Chem. Phys.*, 2019, **150**, 224302.
60 L. J. Criscenti, S. L. Brantley, K. T. Mueller, N. Tsomaia and J. D. Kubicki, *Geochim. Cosmochim. Acta*, 2005, **69**, 2205–2220.
61 T. Bräuniger, P. Kempgens, R. K. Harris, A. P. Howes, K. Liddell and D. P. Thompson, *Solid State Nucl. Magn. Reson.*, 2003, **23**, 62–76.
62 K. Narita, J. Umeda and K. Hazime, .
63 K. T. Mueller, J. H. Baltisberger, E. W. Wooten and A. Pines, *J. Phys. Chem.*, 1992, **96**, 7001–7004.
64 J. L. Bonardet and J. P. Fraissard, *J. Magn. Reson.*, 1976, **22**, 543–548.
65 L. Zhou, M. Leskes, A. J. Ilott, N. M. Trease and C. P. Grey, *J. Magn. Reson.*, 2013, **234**, 44–57.
66 A. Kubo, T. P. Spaniol and T. Terao, *J. Magn. Reson.*, 1998, **133**, 330–340.
67 J. Furrer, K. Elbayed, M. Bourdonneau, J. Raya, D. Limal, A. Bianco and M. Piotto, *Magn. Reson. Chem.*, 2002, **40**, 123–132.
68 A. S. Childress, P. Parajuli, J. Zhu, R. Podila and A. M. Rao, *Nano Energy*, 2017, **39**, 69–76.